ACS Catalysis

Research Article

pubs.acs.org/acscatalysis

# Evolution of High-Energy Electron Beam Irradiation Effects on Zeolite Supported Catalyst: Metal Nanoprecipitation

Kai Song,[†] Dana J. Sauter,[‡] Jinsong Wu,*[,†] Vinayak P. Dravid,[†] and Peter C. Stair[‡]

[†]NUANCE Center and Department of Materials Science and Engineering and [‡]Department of Chemistry, Northwestern University, Evanston, Illinois 60208, United States

**ABSTRACT:** The high-energy electron irradiation effects on Fe-loaded, zeolite-supported catalyst were examined by transmission electron microscopy. In the original sample under little beam irradiation, no nanoparticles larger than 1 nm can be observed, and about half of the loaded Fe is identified as being in a positive ion state (i.e., iron oxides). Metal Fe nanoparticles in neutral state $Fe^0$ were then found to precipitate quickly under beam illumination with an electron dose of ~$2.4 \times 10^7$ $nm^{-2}$ or above at room temperature. Since electron microscopy is widely applied in the characterization of all sorts of catalysts supported on zeolites, the current observations could be treated as a model system to distinguish the metal nanoparticles existing in the original catalyst from those precipitated by electron beam irradiation. It was the ionization effect of electron radiation, other than temperature rise, that played an important role in the formation and growth of the metal precipitates. In the current system, the induced nanoprecipitations were identified as pure Fe metal clusters by electron energy loss spectroscopy (EELS), high-resolution transmission electron microscopy (HRTEM), and electron diffraction. As in current modeling system, although only metal Fe nanoparticles can be observed by EELS if the irradiation effect is ignored at the first place, the functional component in the loaded catalyst is actually a mixture of Fe-oxide and Fe.

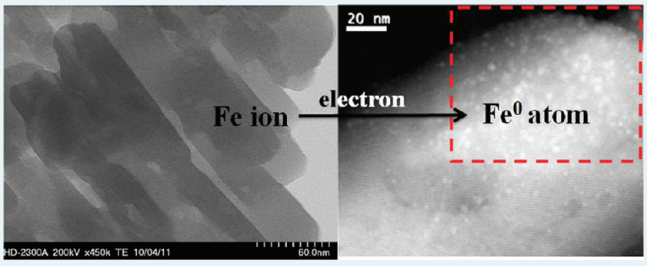


**KEYWORDS:** *metal precipitation, irradiation effects, Zeolite supported catalysis, transmission electron microscopy*

## 1. INTRODUCTION

Zeolites are microporous crystalline aluminosilicates with framework structures composed of $Si(A1)O_4$ tetrahedral units.[1,2] They have the framework structures of submicroscopic, highly uniform channels and pores and are suitable to be used as molecular sieves. Zeolites are commonly used supports for nanoparticle catalysis. It has been found that encapsulating metal-oxide particles inside zeolite cages is essential to having the selective catalytic properties of the metal species.[3,4] Recently, iron-loaded zeolites have attracted lot of interest because of remarkable catalysis properties in the reduction of nitrogen oxide ($NO_x$) emission.[4−9] Long and Yang[6] reported that Fe-ZSM-5 catalyst exhibited remarkably high activities for reducing NO and $NO_2$, which is one of the major sources for air pollution and acid rain. Jisa et al.[7] recently reported superior activity of Fe-FER zeolite for decomposition of nitrous oxide ($N_2O$), a strong greenhouse gas. Qi et al.[8] reported that Fe-exchanged zeolites as catalysts converted over 99% $NH_3$ to $N_2$ and obtained nearly 100% $N_2$ selectivity at 400 °C. It was also found that Fe-zeolites were able to convert $NO_x$ to $N_2$ with high selectivity and activity even in the presence of water.[9] The latter is a useful and important attribute as diesel fuels, and the current modern engine, can contain up to 10% water vapor in the exhaust fumes. The catalytic activity of metal species is system dependent and affected by many factors such as particle size, geometry, composition, oxidation state, and chemical/physical environment.[10] Characterization of the metal nanoparticles, as well as the zeolite, is crucial to understanding the structure function relationship between the metal complexes and its catalytic properties.

Transmission electron microscopy (TEM) has been extensively used for structure analysis of zeolites.[2,11−13] High resolution TEM (HRTEM) has been used successfully to reveal fine structural features such as intergrowths, twinnings, and stacking faults in many zeolites.[11−13] In particular, the most effective technique for detection of the small metal nanoparticles supported on zeolites is scanning transmission electron microscope (STEM) imaging with a high angle annular dark field (HAADF) detector, which shows Z-contrast. Z-contrast is related to atomic number via a square relationship: the higher the elemental number, the brighter it is. This makes it easy to find the heavy metal nanoparticles embedded inside zeolites consisting mainly of light atoms. Furthermore, coupled with electron energy loss spectrometry (EELS) and X-ray dispersive spectrometry (EDX), analytical STEM can not only image the metal nanoparticles but also extract the composition and electronic state of the nanoparticles. The effect of electron irradiation in modifying the structure and property of zeolite had long been observed under S/TEM. It was known that zeolites can be amorphized easily upon electron irradia-

**Received:** January 3, 2012
**Revised:** February 1, 2012
**Published:** February 3, 2012

  

tions.[14−16] The open, cage-like structure of zeolite is susceptible to breakdown if part of the network is disrupted because of ionization. Wang et al.[14] reported that the electron doses for amorphization of three types of zeolites by a 200 keV electron irradiation at room temperature (RT) were from $7.0 \times 10^5$ to $3.4 \times 10^6$ $nm^{-2}$. Typical HRTEM imaging needs an electron flux of about $7.0 \times 10^5$ $nm^2$ $s^{-1}$,[17] which can cause amorphization of most zeolites in a short time. The electron beam irradiation effects on solute were also reported, that is, various types of nanoprecipitation formed out of amorphous or crystalline matrix. Wang et al.[18] observed irradiation-induced three-dimensional nanophase formation by in situ TEM for a number of polycrystalline intermetallic compounds and ceramic materials. Precipitation of amorphous $Si_3N_4$ from supersaturated $\alpha$-Fe solid solution with 1.6 at% Si because of favorable interface energy between the precipitates and the matrix was reported by Mittemeijer et al.[19] Qin et al.[20] reported formation of nanocrystalline Fe−B intermetallic phase by electron beam irradiation from amorphous $Fe_{85}B_{15}$ at a temperature far lower than the thermal crystallization temperature. The structure of the nanoprecipitation depends on many factors such as beam energy, bulk energy of matrix and precipitates, atomic diffusivity, and interface energy. With precise beam control, irradiation-induced nanoprecipitation could be finely controlled for beneficial modifications of the system. For example, Pribytkov et al.[21] reported that electron irradiation of hetereogenous catalysts was a promising method to modify the structure and activity of catalysts by affording new types of active sites on the catalyst surface possessing higher activity and/or selectivity.

Despite many reports on the electron irradiation effect on zeolites, literature reports on effects of electron irradiation on the nanoprecipitation in metal-loaded zeolites in TEM has been surprisingly rare. Considering the extensive application of S/TEM in studies of metal-loaded zeolites and potential system modification, a better understanding of the electron irradiation effects on metal-loaded zeolites is of significance to both fundamental research and practical applications. In this report, we present our observations of electron beam irradiation on Fe-loaded Mordenite (MOR)-zeolite catalyst in S/TEM operating at 200 KV in a temperature range from 100 K to 973 K with either liquid nitrogen cooling sample holder or an in situ heating holder. Fe nanocrystals were observed to precipitate from the Parent Mordenite (MOR) zeolite quickly upon electron irradiation at either low or high temperatures.

## 2. EXPERIMENTAL SECTION

Parent Mordenite zeolites were provided by Dr. Jeffrey Miller of Argonne National Laboratories. The as-received MOR is a one-dimensional (1-D) zeolite with orthorhombic structure and pores sized 6.7 Å in diameter. The proton zeolites (Silica/Alumina ratio = 50) were first calcined at 550 °C for 5 h in a solid state furnace in air to remove the organic framework. Loading of Fe was conducted by the chemical vapor deposition (CVD) method previously described by Chen and Sachtler.[22] The hydrogen zeolite was loaded into a double fritted U-tube reactor on the downstream side. Iron precursor was then loaded onto the other, upstream porous frit, and a dry-argon gas stream (120 mL/min) was flowed through the reactor. Zeolites were heated using heating tape to a temperature of 320 °C for 3−5 h to remove excess water from the zeolite. Next, the iron precursor was heated to the sublimation temperature (100 °C for ferrocene) for 12 h. Finally the whole reactor was heated to the sublimation temperature for 2 h. Loaded zeolites were then washed sufficiently and dried in air at 550 °C for 5 h.

Specimens for S/TEM were prepared by light grinding the catalyst powders in liquid nitrogen using a mortar and pestle. Small amount of dispersed powders separated by boiling liquid nitrogen was picked up by using either copper or nickel TEM grids supported with lacey carbon film. Cooling and heating stages were used for in situ TEM observations at 100 K and at elevated temperatures up to 973 K, respectively. In situ STEM analysis was carried out on a Hitachi HD-2300 STEM operated at 200 KV with probe resolution of 0.34 nm. The STEM images were taken by using either bright-field (phase contrast) or HAADF detector (Z-contrast) with electron flux ranging from $1.0−9.4 \times 10^5$ $nm^{-2}$ $s^{-1}$. Electron energy loss spectrometry (EELS) was conducted with a post column Gatan Enfina EELS spectrometer. The energy resolution of the spectrometer was measured to be about 1 eV for zero-loss peak. X-ray energy dispersion spectrometry (EDX) was conducted using two integrated Thermo Scientific Si(Li) EDX detectors with energy resolution of 129 eV (Mn). In situ TEM experiments were conducted at 100 K, 297 K, 623 K, and 973 K, respectively. HRTEM and selected area electron diffraction (SAED) analysis were carried out to determine lattice structure of the beam-induced precipitates by a JEOL 2100F TEM operated at 200 KV with a lattice resolution of 0.10 nm and a point-to-point resolution of 0.19 nm. For most of the controlled irradiation experiments on the JEOL 2100F TEM, the specimens were first irradiated for 10−20 min under STEM imaging mode with an electron flux of $\sim 2.4 \times 10^6$ $nm^{-2}$ $s^{-1}$. After irradiation, the beam induced precipitation was subject to HRETM and SAED analysis under TEM imaging mode.

## 3. RESULTS AND DISCUSSION

**Precipitation of Nanoparticles.** An overall view of the original Fe-MOR zeolite at room temperature (RT) was shown in Figure 1(a), which is a bright-field STEM image taken at electron flux of $4.1 \times 10^5$ $nm^{-2}$ $s^{-1}$. It can be seen from the lattice fringes that the zeolite has crystalline structure. The original specimen is composed of many rectangular crystalline blocks and plates with sizes of about 0.2 to 1 $\mu$m. One of the magnified Fe-zeolite plates is shown in the inset in Figure.1b. It was taken in HAADF mode on HD-2300 STEM with a low electron flux of $1 \times 10^5$ $nm^{-2}$ $s^{-1}$ immediately after focusing (in several seconds). This was to ensure that the region under examination underwent minimum electron exposure so that the irradiation effect could be minimized. The dark contrast was likely from porosity which was common to this Fe-zeolite.[23] Although Fe content measured by ICP was around 0.8 wt %, no Fe-rich precipitates, which would have appeared as bright spots in Z-contrast STEM, could be observed across the plate. The Fe could be identified by using EELS as shown in Figure 1c, where clear Fe-$L_{23}$ edges could be seen. Details on the quantification of the EELS spectrum will be discussed later along with that of nanoprecipitations.

Figure 2 shows precipitation under irradiation for 60, 150, 390, and 1200 s, respectively, at RT with an electron flux of $4.1 \times 10^5$ $nm^{-2}$ $s^{-1}$ which is in line with those for typical HRTEM conditions. It was found that some nanoparticles appeared in just 60 s of irradiation. In fact, a few nanoprecipitates were observed even as early as during the fine focusing. The precipitates grew larger as irradiation (illumination) proceeded, as shown in Figure 2b−d. EDS results in Figure 3 showed that the precipitates were Fe-rich. Figure 3 shows a comparison


dx.doi.org/10.1021/cs300002c | ACS Catal. 2012, 2, 384−390

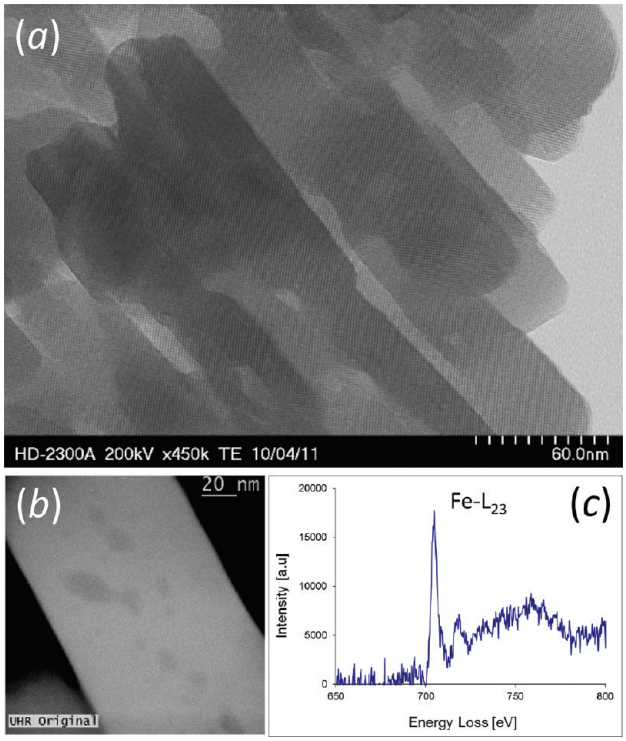


**Figure 1.** (a) BF STEM showing the original Fe-MOR zeolite with minimum beam irradiation. (b) HAADF STEM image on a single plate where no nanoparticles were observed. (c) EELS spectrum obtained from the original Fe-MOR zeolite with minimum beam irradiation showing clearly Fe edges.

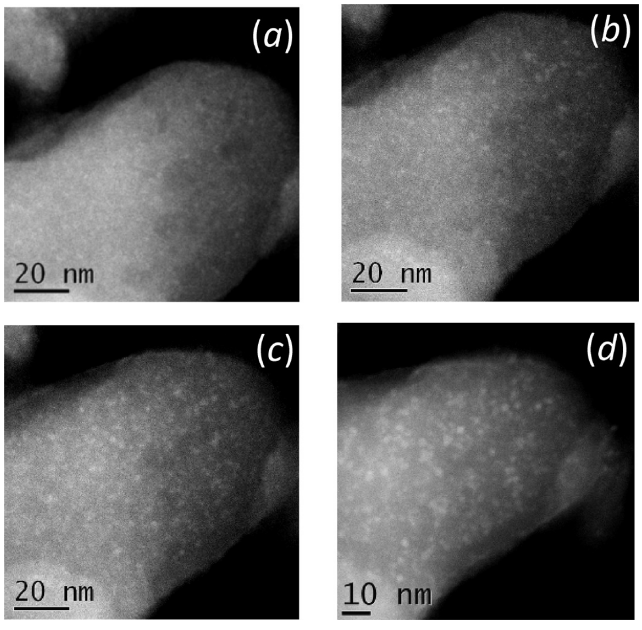


**Figure 2.** HAADF STEM images showing progressive precipitation of Fe-rich nanoparticles at room temperature after electron beam irradiation for (a) 60 s, (b) 150 s, (c) 390 s, and (d) 1200 s.

between the spectra obtained from the precipitates and the zeolite matrix close to them. The spectra were averaged over 12 different locations to reduce noise. The Cu signal was from Cu TEM grid. The dashed line in Figure 3 shows the averaged Fe count measured from the overall original specimen normalized with the Si peak. The fact that the matrix adjacent to the

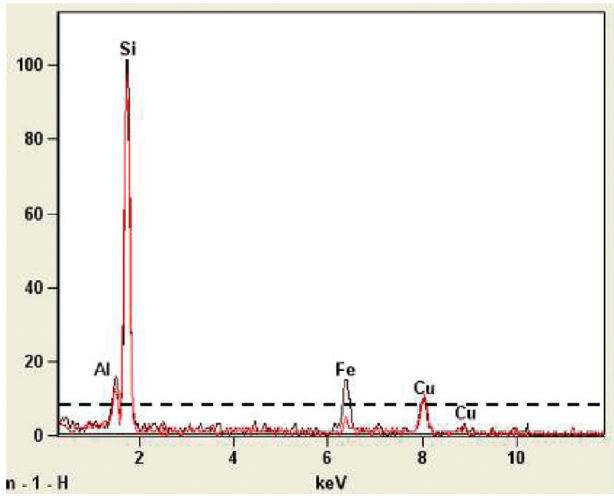


**Figure 3.** Averaged EDX spectrum obtained at RT from 12 nanoparticles and from the matrix close to these particles, respectively. The dashed line indicates Fe intensity obtained from the original specimen normalized by the Si peak.

precipitates had lower Fe intensity than the original specimen could be due to depletion of Fe from the matrix to the precipitates. It is reasonable to infer from Figure 3 that Fe diffused from the rest of matrix into the area where precipitates nucleated and grew during irradiation. Apart from the precipitation, it is worthy to mention that the zeolite rapidly amorphorized upon irradiation, that is, the lattice fringe in Figure 1 completely disappeared within 10 s of irradiation.

We found that the formation of Fe-rich precipitation was a direct result of ionization effect of electron beam irradiation, which played a much more important role than the temperature rise. The Fe-loaded sample was heated up to 973 K inside the microscope, and the regions with different amounts of electron radiation are shown in Figure 4. The region in the upper-right

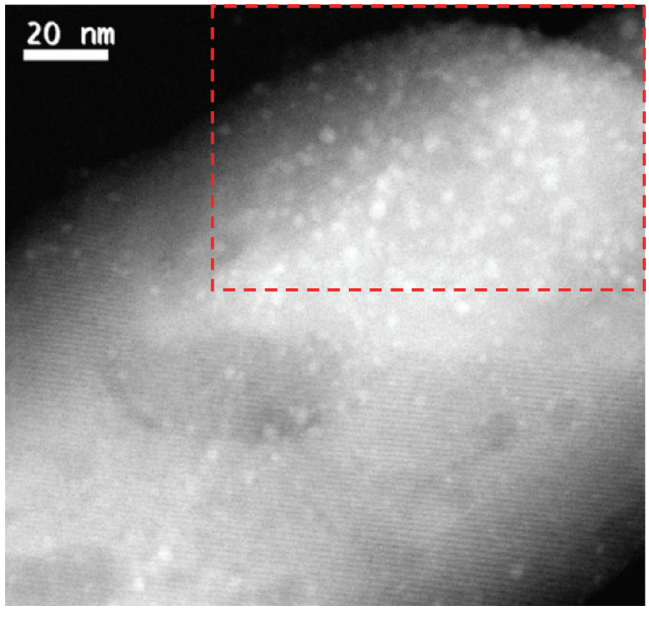


**Figure 4.** HAADF STEM image showing comparison between electron irradiated region (surrounded by the red dashed line) and non-irradiated region at 973 K.


dx.doi.org/10.1021/cs300002c | ACS Catal. 2012, 2, 384–390

corner of Figure 4 (as shown by red dashed line in Figure 4) was illuminated by the electron beam for 10 min while the lower region was excluded from irradiation as much as possible. It is seen that the vast majority of the precipitates were located within the irradiated region. Because of the necessary focusing process, beam spreading, and spurious irradiation in the column, it was impossible to completely exclude electron radiation from the lower region. This could have led to the formation of a few precipitates as well inside the area: the less the beam irradiation, the fewer precipitates formed. Meanwhile, the zeolite in the less-irradiated region still kept a crystalline structure, as indicated by the lattice fringe in Figure 4. It is fair to say that the ionization effect, other than the temperature rise, is the key factor in precipitation nucleation.

**Growth of Nanoparticles.** Furthermore, electron radiation is also important in the growth of nucleated precipitates. In another experiment, one typical region was irradiated for 2 min at 973 K to induce some precipitation. Then the electron beam was removed from this region while the specimen was held for 2 h at 973 K inside the TEM. Figure 5 shows the results before

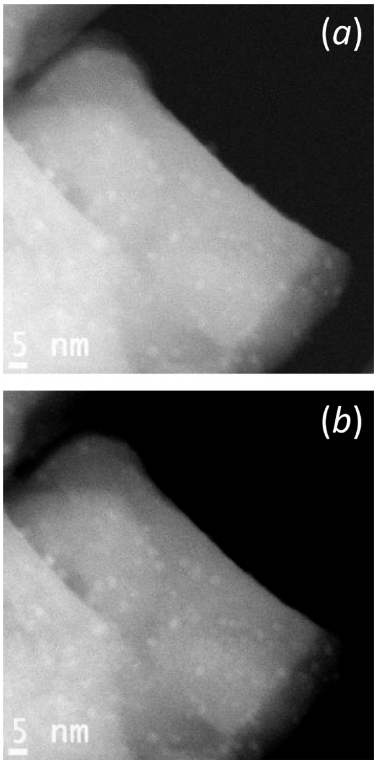


**Figure 5.** (a) Region after 2 min of irradiation showing a few precipitates at 973 K; (b) the same region held at 973 K for 120 min without beam irradiation showing almost identical precipitates.

and after 2 h annealing at 973 K with no beam, and after initial 2 min exposure to the irradiation. It can be seen from the two images that there were almost identical precipitates, which implies that neither new precipitation formed nor did the previously formed nanoparticles grow in 2 h at 973 K without beam irradiation. It was also observed that the MOR zeolite retained crystalline structure at a temperature range from 100 K to 973 K when there is no electron beam irradiation. It is likely that the loss of crystalline structure in the zeolite matrix could prompt the diffusion of metal atoms which accelerated the formation and growth of the nanoparticles.

The observed nanoprecipitation was likely diffusion-controlled which involved long-range Fe redistribution across the zeolite matrix. The diffusion-controlled growth rate for small spherical precipitates can be expressed as[24]

$$d^2 - (d^*)^2 = D\varpi \times t \quad (1)$$

where $d$ is average particle size, $d^*$ is the critical size when the precipitates nucleate at $t = 0$, $D$ is effective diffusion coefficient, and $\phi$ is dimensionless supersaturation. The size distributions of the nanoparticles for various durations and temperatures were measured in this study. A typical size distribution of the precipitates formed at RT after 20 min of irradiation is shown in Figure 6. A statistical analysis of 93 particles exhibits a size

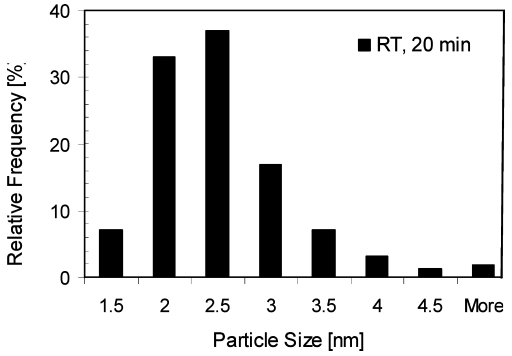


**Figure 6.** Typical particle size distribution for the irradiation-induced precipitation. The sample was irradiated at RT for 20 min.

distribution peaking around 2.3 nm, with a standard deviation of 0.66 nm.

The square of the average particle size against irradiation time (with normalized electron flux of $7 \times 10^5$ nm$^{-2}$ s$^{-1}$) is plotted in Figure 7a for temperatures of 100, 298, 623, and 973 K. It is found that at each temperature, the particle growth was initially fast, then slowed down, and finally stagnated at a rather stable size after about 30 min of irradiation. Even at a low temperature of 100 K, precipitates with a size larger than 1 nm were observed within 1 min of irradiation. The initial stage of the precipitate growth (up to 10 min) obeyed the parabolic growth law of diffusion-controlled growth (eq 1). The critical precipitate nucleation size at extrapolated zero time is around 1.5 nm, which increased slightly with temperature. It is noted that the slope, $D\phi$, increases with temperature in Figure 7a. As $\phi$ does not vary with temperature, the increase in slope is due to an increase in Fe diffusivity at high temperature. Figure 7b shows the experimental values of $D\phi$ as a function of $1/T$. It can be seen that the growth parameter $D\phi$ does not obey a simple Arrhenius relationship. In fact, the growth parameter showed only a moderate increase from 0.14 at 100 K to 0.62 at 973 K. This is by no means close to the exponential increase, which would be expected for a thermally controlled diffusion. The activation energy of Fe in Fe-rich amorphous alloys was reported to be about 1.5 eV.[25,26] If the Fe diffusion in amorphous zeolites had been thermally controlled, the increase in Fe diffusivity, and thus the growth parameter, should have increased by tens of orders of magnitude when the temperature rose from 100 K to 973 K, rather than a negligible 4-fold increase as was experimentally observed. Considering the fact that precipitation nucleation and growth also only occurred in the irradiated region, it is concluded that the observed Fe diffusion was not thermally controlled. This agrees with


dx.doi.org/10.1021/cs300002c | ACS Catal. 2012, 2, 384−390

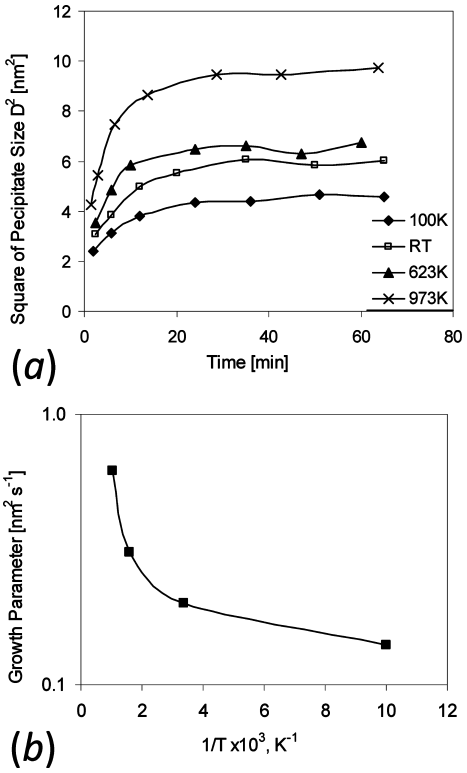


**Figure 7.** (a) Growth of the nanoparticles vs irradiation time at 100, 298, 623, and 973 K. (b) Dependence of the precipitate growth parameter, $D\phi$, on inverse temperature.

literature reports that the irradiation-induced nanocrystallization from amorphous alloys is often isothermal in nature. For example, Qin et al. described[20] irradiation-induced crystallization of amorphous $Fe_{85}B_{15}$ alloy at temperatures much lower than required for thermal crystallization. It has been reported[27,28] that high-energetic irradiation can substantially enhance the atomic diffusivity in the amorphous state and assist short-range order even at liquid nitrogen temperature. Apart from these, the crystalline structure of the zeolites, in which metal atoms are located, may have limited the Fe diffusivity. As shown in Figure 4, the crystalline structure of the zeolite was not modified even after heating at 973 K, but easily transformed into amorphous structure upon electron irradiation. It is also observed in Figure 7a that the irradiation-induced precipitate growth stagnated after about 30 min of irradiation, which deviates from the classical parabolic growth. After certain time, Fe could not be supplied to the irradiated region where the matrix was gradually depleted of Fe during the precipitation process. After the majority of iron had been depleted from the matrix, the growth of the nanoparticles virtually stopped. In short, we found that in the current Fe-loaded zeolite the growth of the nanoparticles was controlled by beam irradiation-induced diffusion, other than by thermally controlled diffusion.

**Identification of Nanoparticles.** It was shown in Figure 3 that the irradiation-induced nanoparticles were Fe-rich. The nature of the precipitates, whether they were crystalline or amorphous, iron or iron-oxide compounds, was not clear. We then characterized the irradiation-induced Fe-rich precipitates by using EELS, HRTEM, and SAED.

We applied EELS to identify the Fe oxidation state of the irradiation-induced nanoparticles. It has been previously reported that Fe atoms of different oxidation state exhibit different intensity ratio of the white lines of the Fe $L$-ionization edge (Fe $L_2$ and $L_3$).[29−31] Table 1 summarizes the literature

**Table 1. Values of Fe-$L_3$ upon Fe-$L_2$ for Fe, $Fe_2O_3$, $Fe_3O_4$, and FeO Reported in Literature**

| literature | Fe | $\alpha$-$Fe_2O_3$ | $\beta$-$Fe_2O_3$ | $Fe_3O_4$ | FeO |
|---|---|---|---|---|---|
| $L_3/L_2$ | 2.0 | 6.0 | 5.5 | 5.2 | 4.6 |
| $L_2$-$L_3$ | ~12.2 | 13.0 | 13.0 | 12.9 | 12.9 |

data on $L_3/L_2$ intensity ratio for Fe, FeO, $Fe_2O_3$, and $Fe_3O_4$.[29,30] The $L_3/L_2$ intensity ratio ranges from 2 for Fe to 6 for $\alpha$-$Fe_2O_3$. A typical EELS spectrum obtained from an irradiation-induced nanoparticle was shown in Figure 8a. The

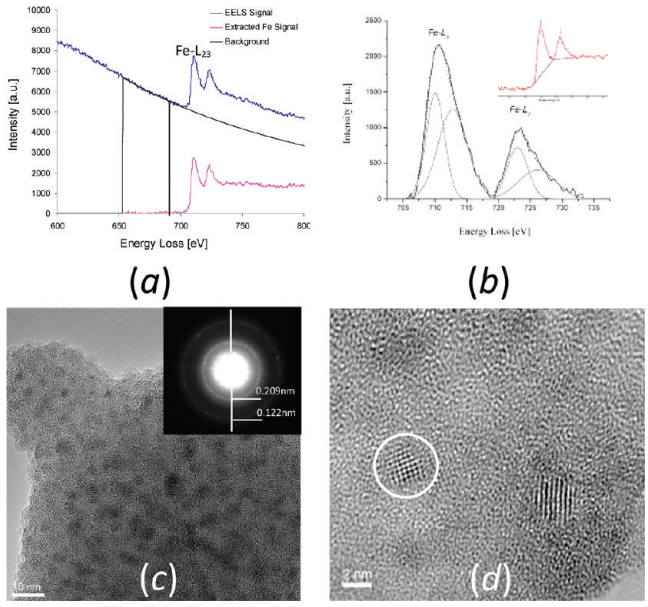


**Figure 8.** (a) Typical EELS spectrum obtained from an irradiation-induced nanoparticle; (b) Quantification of the Fe-$L_{32}$ lines using Pearson's method. The inset showing subtraction of background below Fe-$L_{32}$ lines; (c) BF image of an irradiated region with SAED pattern (inset, left); (d) HRTEM image of the irradiation-induced nanoparticles (among which one is circled).

spectrum has an energy dispersion of 0.3 eV and contains the iron $L_{23}$-ionization edges. The ionization edge of Fe sits on a strong background which must be removed before quantification. This was done by using the standard power law method provided in the Gatan Digitalmicrograph software. The pre-edge energy window selected for the fitting, traces of fitted curve, and the extracted signal after background removal were also drawn in Figure 8a. To quantify the iron $L_{23}$-edge and to measure the $L_3/L_2$ intensity ratio, the method developed by Pearson[32] was used in this study. A linear function was fitted from the edge onset to the first minimum to subtract the background below the $L_3$- line, and a second linear function was fitted from the first to the second minimum to subtract the background below the $L_2$-line, as shown in the inset in Figure 8b. Subsequently, two Gaussian peaks were fitted to each line to account for the line asymmetry. The two Gaussian peaks had better fitting to account for the edge asymmetry than single Gaussian or Lorentzian fitting.[29] The peak fitting was conducted using XI-SDP 4.3 software. The intensity of each L-line was then calculated by adding the areas below the two


dx.doi.org/10.1021/cs300002c | ACS Catal. 2012, 2, 384−390

corresponding Gaussian peaks, as shown in Figure 8b. EELS spectra were collected from those particles near the thin edge of zeolite to enhance matrix Fe depletion and minimize any remaining contribution of Fe signal from the zeolite matrix. The Fe $L_3/L_2$ intensity ratio in Figure 8d was measured to be 2.03. To increase statistical reliability, EELS data were collected from 15 nanoparticles formed in different zeolite blocks after irradiation. Their EELS spectra were quantified similarly using the Pearson's method. It was found that the measured $L_3/L_2$ intensity ratios of the 15 particles have an average of 2.06 with a rather small standard variation of 0.12. Therefore, the EELS results gave further evidence that the irradiation-induce precipitates observed in this study are pure metal Fe. Similar quantitative analysis has been applied to the EELS spectrum obtained from the original sample with very little electron beam irradiation as shown in Figure 1c. The measured $L_3/L_2$ intensity ratio of the original sample is 3.5. A straightforward interpretation of the value is that almost half the Fe atoms in the original sample exist as positive ions, mostly likely bonded with oxygen by forming iron oxides.

The nanoprecipitation was studied by using HRTEM and electron diffraction. Figure 8c shows a TEM image of nanoparticles formed after 20 min of irradiation at RT. The inset in Figure 8c is the corresponding SAED pattern. The two rings in the pattern correspond to spacing of 0.209 and 0.122 nm, respectively, which in principle can be indexed by either body-centered cubic (*bcc*) or face centered cubic (*fcc*) Fe lattice. The slightly diffuse appearance of the rings was a result of the nanometer size of the particles. Figure 8d is a HRTEM image of the irradiation-induced nanoparticles of about 2−3 nm; the crystalline lattice can be clearly seen (i.e., the circled nanoparticles in the figure). The structure of metal nanoparticles smaller than 2−3 nm may be complex polyhedrons since large portion of the atoms are on the surface,[33] before they can be slowly evolved into a defined lattice with either *bcc* or *fcc* structure.

## 4. CONCLUSIONS

Fe-MOR zeolite was subjected to electron irradiation at temperatures from 100 K to 973 K in S/TEM operating at 200 KV. While no nanoparticles larger than 1 nm could be observed under a low-dose imaging condition, Fe nanoparticles of 2−3 nm were found to form quickly under common imaging conditions inside S/TEM at all temperatures. In the original sample, about half of the Fe atoms are positive ions bonded with oxygen. After beam irradiation, the Fe-rich precipitates were neutral Fe as measured by EELS indicating that Fe-ions have been reduced. The precipitation was strictly confined to the irradiated region. The irradiation-induced precipitation growth obeyed a parabolic law in the beginning, and was controlled by beam irradiation-induced diffusion, other than by thermally controlled diffusion. The precipitation growth stagnated after about 30 min of irradiation because of depletion of Fe from the matrix. HRTEM and diffraction analysis show that the precipitates are crystalline. As electron microscopy is an effective and widely used method in catalyst characterization, the effect of electron irradiation should be taken into consideration to correctly interpret S/TEM observations.

## AUTHOR INFORMATION

### Corresponding Author

*E-mail: jinsong-wu@northwestern.edu.

### Notes

The authors declare no competing financial interest.

The research is supported by Northwestern University's Center for Catalysis and Surface Science, Office of the Vice President for Research.

## ACKNOWLEDGMENTS

This work was supported by the U.S. Department of Energy, Office of Basic Energy Science, Chemical Sciences under contract DE-FG02-03-ER15457. The electron microscopy work was performed in the Electron Probe Instrumentation Center (EPIC) facility of NU*ANCE* Center (supported by NSF-NSEC, NSF-MRSEC, Keck Foundation, the State of Illinois) at Northwestern University.

## REFERENCES

(1) Auerbach, S. M.; Carrado, K. A.; Dutta, P. K. *Handbook of Zeolite Science and Technology*; CRC Press: Boca Raton, FL, 2003; Chapter 1.
(2) Pan, M. *Micron* **1996**, *27*, 219−238.
(3) Boreskov, G. K. *Heterogenous Catalyst*; Nova Science Publishers: Hauppauge, NY, 2003; Chapter 5.
(4) Valtchev,V.; Mintova, S.; Tsapatsis, M. *Ordered Porous Solids−Recent Advance and Prospects*; Elsevier B.V.: Amsterdam, The Netherlands, 2009; Chapter 28.
(5) Bitter, J. H.; Battiston, A. A.; van Donk, S.; de Jong, K. P.; Koningsberger, D. C. *Microporous Mesoporous Mater.* **2003**, *64*, 175−184.
(6) Long, R. Q.; Yang, R. T. *J. Am. Chem. Soc.* **1999**, *121*, 5595−5596.
(7) Jisa, K.; Novakova, J.; Schwarze, M.; Vondrova, A.; Sklenak, S.; Sobalik, Z. *J. Catal.* **2009**, *262*, 27−34.
(8) Qi, G.; Gatt, J. E.; Yang, R. T. *J. Catal.* **2004**, *226*, 120−128.
(9) Gao, Z-X; Sun, Q.; Sachtler, W. M. H. *Appl. Catal., B* **2001**, *33*, 9−23.
(10) Cuenya, B. R. *Thin Solid Films* **2010**, *518*, 3127−3150.
(11) Thomas, J. M.; Terasaki, O.; Gai, P. L.; Zhou, W. Z.; Gonzalez-Calbet, J. *Acc. Chem. Res.* **2001**, *34*, 583−594.
(12) Terasaki, O.; Ohsuna, T.; Alfredsson, V.; Bovin, J.-O.; Watanabe, D.; Tsuno, K. *Ultramicroscopy* **1991**, *39*, 238−246.
(13) Terasaki, O.; Ohsuna, T. *Catal. Today* **1995**, *23*, 201−218.
(14) Wang, S. X.; Wang, L. M.; Ewing, R. C. *J. Nucl. Mater.* **2000**, *278*, 233−241.
(15) Yuan, Z.-Y.; Zhou, W.; Parvulescu, V.; Su, B.-L. *J. Electron Spectrosc. Relat. Phenom.* **2003**, *129*, 189−194.
(16) Yokota, Y.; Hashimoto, H.; Yamaguchi, T. *Ultramicroscopy* **1994**, *54*, 207−214.
(17) Wang, C. M.; Baer, D. R.; Amonette, J. E.; Engelhard, M. H.; Antony, J. J.; Qiang, Y. *Ultramicroscopy* **2007**, *108*, 43−51.
(18) Wang, L. M.; Wang, S. X.; Ewing, R. C.; Meldrum, A.; Birtcher, R. C.; Provencio, P. N.; Weber, W. J.; Matzke, H. J. *Mater. Sci. Eng.* **2000**, *A286*, 72−80.
(19) Mittemeijer, E. J.; Biglari, M. H.; Bottger, A. J.; van der Pers, N. M.; Sloof, W. G.; Tichelaar, F. D. *Scr. Mater.* **1999**, *41*, 625−630.
(20) Qin, W.; Nagase, T.; Umakoshi, Y. *Acta Mater.* **2009**, *57*, 1300−1307.
(21) Pribytkov, A. S.; Tkachenko, O. P.; Stakheev, A. Y.; Klementiev, K. V.; Grunert, W.; Maurits, W.E.V.D.B.; Kustov, L. M.; Golubeva, V. N.; Tel'nov, A. V. *Mendeleev Commun.* **2006**, *16*, 254−256.
(22) Chen, H.-Y.; El-Malki, El-M.; Wang, X.; van Santen, R. A.; Sachtler, W. M. H. *J. Mol. Catal A: Chem.* **2000**, *163*, 159−174.
(23) Rollman, L. D.; Valyocsik, E. W. U.S. Patent 4 205 052 (1980), to Mobil Oil Corporation.
(24) Sun, W. P.; Militzer, M.; Jonas, J. J. *Metall. Trans. A* **1992**, *23*, 3013−3023.
(25) Wurschum, R.; Herth, S.; Brossmann, U. *Adv. Eng. Mater.* **2003**, *5*, 365−372.
(26) Gupta, M.; Gupta, A.; Rajagopalan, S.; Tyagi., A. K. *Phys. Rev. B* **2002**, *65*, 214204.

(27) Kopcewicz, M.; Dunlop, A. *J. Appl. Phys.* **2001**, *90*, 74−80.
(28) Bellini, S.; Montone, A.; Vittoriantisari, M. *Phys. Rev. B* **1994**, *50*, 9803−9809.
(29) Jasinski, J.; Pinkerton, K. E.; Kennedy, I. M.; Leppert, V. J. *Microsc. Microanal.* **2006**, *12*, 424−431.
(30) Wang, F.; Malac, M.; Egerton, R. F. *Micron* **2006**, *37*, 316−323.
(31) Colliex, C.; Manoubi, T.; Ortiz, C. *Phys. Rev. B* **1991**, *44*, 11402−11411.
(32) Pearson, D. H.; Fultz, B.; Ahn, C. C. *Appl. Phys. Lett.* **1988**, *53*, 1405−1407.
(33) Jadzinsky, J. D.; Calero, G.; Ackerson, C. J.; Bushnell, D. A.; Kornberg, R. D. *Science* **2007**, *318*, 430−433.